Journal of Materials Chemistry A

ROYAL SOCIETY OF CHEMISTRY

PAPER

View Article Online
View Journal

Cite this: DOI: 10.1039/d0ta03416a

Maximizing piezoelectricity by self-assembled highly porous perovskite–polymer composite films to enable the internet of things†

Asif Abdullah Khan, [a] Md Masud Rana,[a] Guangguang Huang,*[a] Nanqin Mei,[b] Resul Saritas,[c] Boyu Wen,[a] Steven Zhang,[a] Peter Voss,[d] Eihab-Abdel Rahman,[c] Zoya Leonenko,[b] Shariful Islam[d] and Dayan Ban*[a]

There is an urgent demand in the industry for the development of compact, flexible, and sustainable power sources for self-powered internet of things (IoT) micro/nano devices. One of the most promising routes is to harness environmental energy through piezoelectric nanogenerators (PNGs). A novel, self-assembled, highly porous perovskite/polymer (polyvinylidene fluoride (PVDF) in this case) composite film was developed for fabricating high-performance piezoelectric nanogenerators (PNGs). The macroscopic porous structure can significantly enlarge the bulk strain of the piezoelectric composite film, which leads to a ≈5-fold enhancement in the strain-induced piezo potential. In addition, the novel hybrid halide perovskites (HHP)–formamidinium lead bromine iodine ($FAPbBr_2I$) material can improve the conductivity of the final composite film due to its enhanced permittivity, providing a ≈15-fold amplification of the output current. Using these highly-efficient perovskite/polymer PNGs (P-PNGs), a peak output power density of 10 μW cm^{-2} (across a resistance of 7 MΩ) was obtained to run a self-powered integrated wireless electronic node (SIWEN). The P-PNG application was then extended to real-life scenarios including wireless data communication between the nanogenerators and personal electronics, efficient energy harvesting from automobile vibrations and also from biomechanical motion. This P-PNG based on a low-temperature full-solution synthesis approach, may initiate a paradigm shift by opening the realms of flexible PNGs as sustainable power sources.

Received 26th March 2020
Accepted 15th May 2020

DOI: 10.1039/d0ta03416a

rsc.li/materials-a

1. Introduction

Developing increasingly compact structures and high performing sustainable power sources has become an important area of research focus to help in the deployment of self-powered electronics. Piezoelectric nanogenerators (PNGs), composed of flexible and compact structures, have emerged as a promising candidates for this purpose.[1] To name a few applications, PNGs have found importance in self-powered nanoelectromechanical systems (NEMS), electronic/piezotronics devices, and implantable medical devices and remote sensing.[2–8]

Altering the microstructures of piezoelectric films to enhance the strain-dependent piezoelectric polarization has proven to be an effective energy-harnessing mechanism. For instance, adopting nanowires,[9–12] aspect ratio tuning, film porosity modulation through a multi-stage etching process,[13–18] cascading multiple devices,[19–22] and reducing charge screening effects[22–27] are remarkable structure-driven techniques, further pushing the piezoelectricity limit. By creating pores in ZnO nanowires,[13] Su *et al.* demonstrated ≈23-fold boosted output current in the PNGs (27.7 nA), with an elevated porosity percentage of 5.4%. By using random and highly porous (50%) polyvinylidene fluoride (PVDF) structures[14] (through etching process), Mao *et al.*[14] enhanced the output voltage and current of the PNG to 11.1 V and 9.7 μA, respectively, which is higher than those of a lithography assisted porous PVDF nanowire array.[9] Recently, Yuan *et al.* presented a cascade type 6-layer rugby-ball-shaped PNG structure and improved the output performance to 88.62 V_{PP} and 353 μA, which is a new record value for multilayer PNGs.[19] Although piezoelectricity can be enhanced by these strategies, optimally unifying appropriate mechanical and electrical properties in a single piezoelectric film still remains to be a challenge.

Among the piezoelectric materials, the single crystals such as lead zirconium titanate (PZT), $(1-x)Pb(Mg_{1/3}Nb_{2/3})O_3$–$xPbTiO_3$ (PMN–PT)[28] are highly desirable as it possess very high

[a]Department of Electrical and Computer Engineering, University of Waterloo, 200 University Ave, Waterloo, ON, Canada. E-mail: g43huang@uwaterloo.ca; dban@uwaterloo.ca

[b]Department of Physics & Astronomy, University of Waterloo, 200 University Ave, Waterloo, ON, Canada

[c]Department of Systems Design Engineering, University of Waterloo, 200 University Ave, Waterloo, ON, Canada

[d]Shimco North America Inc., 75 Heroux Devtek Dr, Cambridge, ON, Canada

† Electronic supplementary information (ESI) available. See DOI: 10.1039/d0ta03416a

piezoelectric coefficient (d_{33}). But the high temperature material synthesis, brittleness, and the presence of toxic lead are the major limiting factors to be used in the PNGs. Thus, developing lead-free piezoelectric materials is an alternative and promising route for fabricating environment-friendly PNG, but the output performance of such materials still remains modest.[29] By dispersing highly piezoelectric NPs in a flexible polymer, composite films can be developed, which is proven to be an attractive, yet easier approach in terms of the fabrication scalability, device flexibility, improved mechanical strength, and enhanced electrical output.[30–34] Nevertheless, nanoparticle (NP) dispersion promoters had to be employed to improve the homogeneous dispersion of the NPs in a polymer scaffold (such as PVDF),[35–40] which adversely impacts device performance. As a trade-off, this issue was addressed by functionalizing the surface of piezoelectric NPs before mixing with polymer[41] or replacing NPs with organic–inorganic metal halide perovskites (OMHPs).[42] By mechanically reinforcing a polymer scaffold (PVDF) with the homogeneously dispersed formamidinium lead halide ($FAPbBr_3$), Ding *et al.* recorded (the highest output of this type) a piezo-potential of 30 V and current density of 6.2 μA cm^{-2}, incorporating an applied pressure of 0.5 MPa.[43] By optimally quantifying the content of uniformly distributed methylammonium lead iodine ($MAPbI_3$) in the PVDF matrix, a cost-effective solution approach for the $MAPbI_3$–PVDF piezoelectric composites was also introduced as a result.[44] In this process, a similar approach stems from changing the polymer to polydimethylsiloxane (PDMS), but it still possesses a detrimental brittleness issue.[45] Moreover substituting the atomic constituents of the OMHP, the piezoelectric and ferroelectric properties can be tuned, and exciting experimental investigations are underway to reliably implement them in practical PNG applications.

In this work, we reported a novel self-assembled highly porous perovskite/polymer composite film *via* the simultaneous control of film structure and material design, which can be used for the PNG applications. The composition of a polymer (PVDF) with a novel hybrid halide perovskite–$FAPbBr_2I$, can significantly enlarge the bulk film strain by forming self-assembled high-density and ordered pores, and can reduce the film impedance due to the high relative permittivity of $FAPbBr_2I$. Consequently, the output voltage and current of the developed P-PNG device dramatically increased by ≈5 times (to ≈85 V peak to peak), and ≈15 times (to ≈30 μA peak-to-peak), respectively over pure PVDF-based PNGs, with an acceleration of 2 G and proof mass of 138 g. Notably, the composite film can be prepared in a one-step manner as the incorporation of multiple nanostructure building blocks, the NP surface functionalization, and follow-up chemical etching all become unnecessary, greatly simplifying the film preparation process and as a result lowering the cost at the same time.

The PNG-driven SIWEN demonstrated in wireless communication between the P-PNG sensors and personal electronics (mobile phones), which is significant for the applications such as self-powered IoT devices, health monitoring of aerospace structures, and implantable biomedical devices. The demonstrated applications also include harnessing tiny mechanical vibrations from a running automobile car engine to efficiently charging up energy storing capacitors and monitoring the engine states by the P-PNG, as well as harvesting energy from biomechanical energy sources (*e.g.* human hand-tapping) to directly drive light-emitting diodes (LEDs).

2. Results and discussion

2.1 Device structure and working mechanism of P-PNGs

The piezoelectric potential is critically affected by the internal pores, as they can redistribute the mechanical strain profile inside the film. By mixing $FAPbBr_2I$ perovskite with PVDF, a new class of piezoelectric films are developed, which takes advantage of the enhanced strain from the internal pore microstructures and the beneficial properties of the novel hybrid lead halide perovskite. A $FAPbBr_2I$ perovskite precursor solution (20 wt%) was synthesized at 60 °C from a homogeneous mixture of formamidinium iodide (FAI) and lead(II) bromide ($PbBr_2$) powder in *N*,*N*-dimethylformamide (*N*,*N*-DMF). The $FAPbBr_2I$ precursor solution was diluted in 10 wt% PVDF, and drop casted on a glass substrate followed by a one-step annealing at 120 °C. Moreover, to align the dipoles a high voltage electrical poling was performed for 2–3 hours with an electric field of 50–120 V μm^{-1} by sandwiching the film between two gold electrodes placed inside a vacuum box. Fig. 1a depicts a schematic illustration of the final device fabrication step, where the composite film is sandwiched between two copper electrodes and is encapsulated between polyester substrates, through a thermal lamination process. To elucidate the perovskite crystal formation inside PVDF, XRD scans over a wide range (diffraction angle 2θ ranging from 10 to 50 degrees) were conducted. The major diffraction peaks appear in Fig. 1b at diffraction angles (2θ) of 14.64, 29.43, 33, 42.12 and 44.39 can be assigned to the (100), (220), (222), (224) and (300) crystal planes of a cubic perovskite structure, respectively. It is noteworthy to mention that replacement of MA with FA cation in the $FAPbBr_2I$ crystal, greatly enhance the structural stability, which is more suitable for the PNG device fabrication. Since it is well known that semi-crystalline PVDF polymer has four distinct phases (α, β, γ and δ) where β-phase is the only one that possess the highest spontaneous polarization, the existence of β-phase can be confirmed by the Fourier transform infrared (FTIR) spectrum. The FTIR spectrum in Fig. 1c demonstrates that, compared with the conventional pure porous PVDF,[46,47] the coherently grown films of $FAPbBr_2I$ crystals with polymer PVDF, have a higher intensity at a wavenumber of ≈475 cm^{-1}, and a similar intensity at 840 cm^{-1}. This result is attributed to the improved β-phase crystallinity of the PVDF, due to the existence of dipolar interactions between the FA^+ cations of $FAPbBr_2I$ and the anionic fluorine ($-CF_2-$) groups of the PVDF.[48,49] The piezoelectric coefficient (D_3) of the composite films can be written as

$$D_3 = \alpha_1 L_E \varphi d_1 + \alpha_2 (1 - \varphi) d_2 \quad (1)$$

where α_1 and α_2 are the poling rate, d_1 and d_2 are the piezoelectric coefficients of different materials in the composite film, respectively, L_E is the local field coefficient and φ is the mass

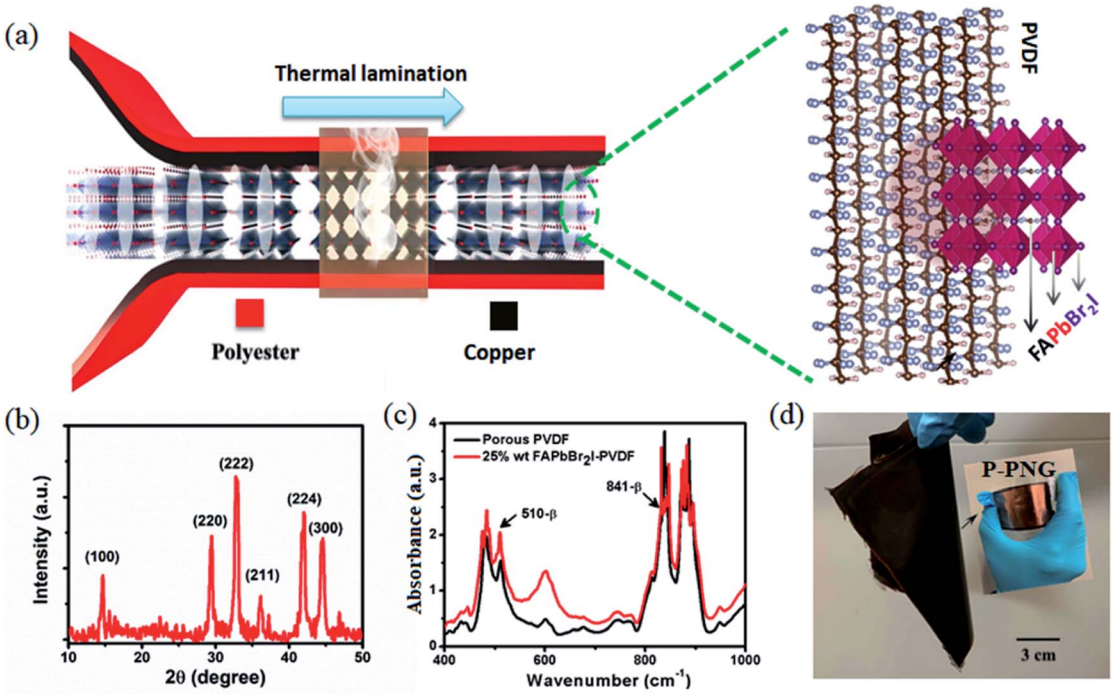

Fig. 1 Device structure of P-PNGs (a) fabrication process of P-PNGs; (b) XRD patterns of 20 wt% $FAPbBr_2I$@PVDF composite film; (c) FTIR results of porous PVDF and $FAPbBr_2I$@PVDF composite films (25 wt%); (d) digital photos of the large area composite film (15 cm × 15 cm) and the fabricated P-PNGs.

fraction. Assuming organic and inorganic phases are fully poled, *i.e.*, $\alpha_1 = \alpha_2 = 1$, and $\varphi = 0.2$, the piezoelectric coefficient D_3 can be estimated. The local electric field ($L_E = 3\varepsilon/(2\varepsilon + \varepsilon_c)$) is related to the relative permittivity of the $FAPbBr_2I$ nanoparticles (ε_c) as well as the composite film (ε).

A previous report suggested that the ε_c can reach to 1000, which is much larger than ε. Therefore, L_E is estimated to be approximately 0.1–0.3.[50] It has been identified that the piezoelectric coefficients of the PVDF and $FAPbBr_2I$ phases are opposite. The approximated D_3 is calculated to be -23 pm V^{-1} when taking $d_1 \approx 25$ pm V^{-1} and $d_2 \approx -29$ pm V^{-1}.[43] Moreover, other predominant factors such as the nanoparticles distribution and film geometry also significantly influence the piezoelectricity of this complex hybrid composite material system. The scalable $FAPbBr_2I$@PVDF composite film (15 cm × 15 cm) and a fabricated flexible P-PNG device are shown in Fig. 1d. From the cross-section of the film, demonstrated by the scanning electron microscopy (SEM) image in Fig. 2a, an array of almost periodic vertical pores were observed. In contrast to a solid and conventional porous PVDF film (Fig. S1 and S2, ESI†), a uniquely self-assembled and highly porous structures were found in the $FAPbBr_2I$@PVDF composite film (material synthesis are described in the experimental Section 4.1, 4.2 & 4.3). The pores are ≈20–25 μm in length (SEM image in Fig. S3a, ESI†) and approximately ≈3–5 μm in diameter (atomic force microscopy (AFM) image in Fig. S3b, ESI†). During the crystallization process, phase separation usually plays an important role in the formation of these porous structures in the composite film. As a result, the crystallization process of PVDF@$FAPbBr_2I$ can be divided into the following two stages.[51] During the first stage (schematic illustration in Fig. S4a, ESI†) (i) while heating up the solution at 60 °C, the *N*,*N*-DMF solvent starts to evaporate and the PVDF crystallizes due to its relatively lower solubility. Then it transforms to a colourlerss film and remains in an intermediate state. (ii) After that, the $FAPbBr_2I$ solution begins to approach to its supersaturated concentration (C_0) and then forms into nanoparticles, which is indicated by the change in colour from colourless to red. The keys to the self-assembly process of $FAPbBr_2I$ nanoparticles embedded into the PVDF scaffold are two different crystallization processes of the PVDF and the $FAPbBr_2I$. During the second stage, the strong interactions between NH^{3+} in the formamidinium (FA) cations of the $FAPbBr_2I$ and $-CF_2-$ groups of the PVDF, the perovskites nanoparticles tend to anchor on the PVDF scaffold. This interaction is reflected by the blue-shift of the infrared absorption peaks of C–F bond in the wave number range of 1350–1100 cm^{-1} (FTIR spectrum in Fig. S4b, ESI†) due to the decreased force constant according to the expression of $\nu = 1304\sqrt{(k/u)}$ (cm^{-1}), where ν is the frequency, k the force constant (N m^{-1}) and u the effective mass. In addition, this interaction can also be observed from the mapping of the fluorine (F) atoms and lead (Pb) atoms which corresponds to the PVDF polymer chain (Fig. 2b) and the $FAPbBr_2I$ crystal (Fig. 2c).

The perovskite clusters (in Fig. 2c) are attached with the PVDF polymer because of their common solubility in the DMF solvent (two materials can grow in one step) and the dipolar interactions between NH_3^+ in FA (perovskite) and $-CF_2-$ groups of the PVDF.

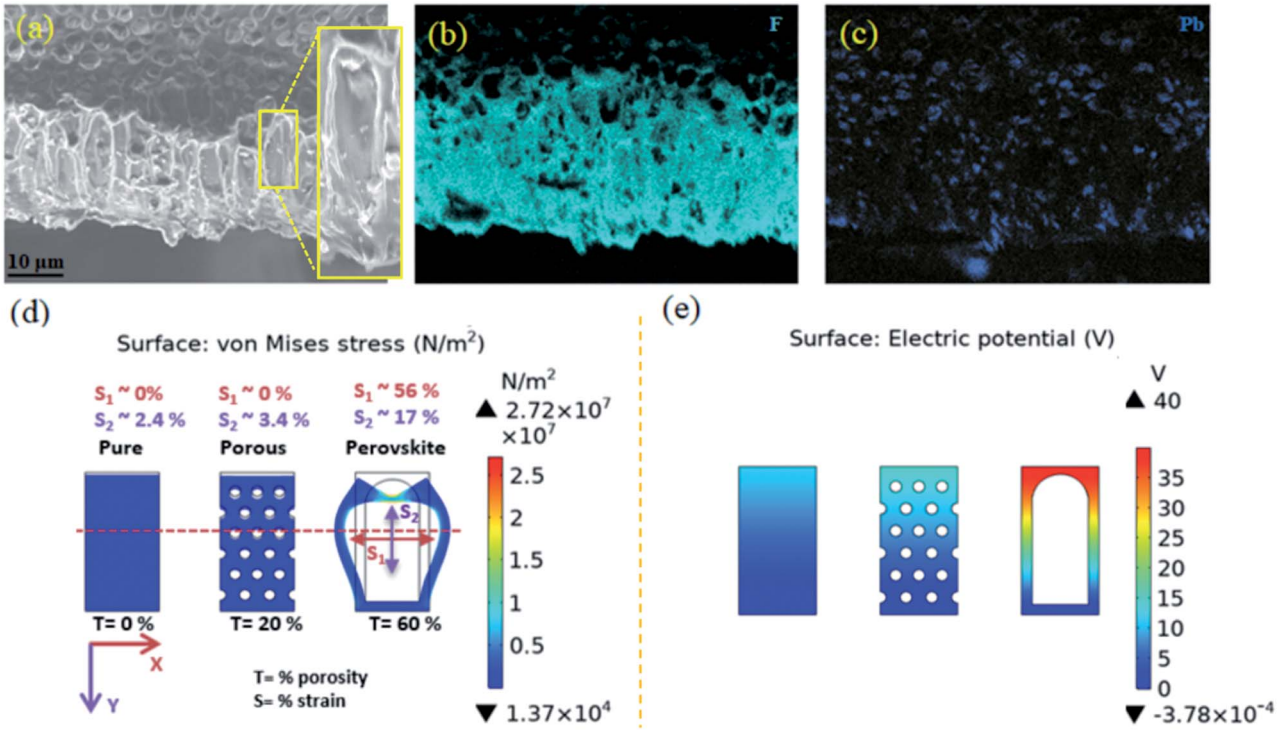

Fig. 2 Working mechanism of P-PNGs (a) cross-sectional SEM image of the self-assembled highly porous PVDF@$FAPbBr_2I$ (20 wt%) composite films (inset shows the close view of a pore); the corresponding element mapping of (b) fluorine (F) in PVDF and (c) lead (Pb) in $FAPbBr_2I$; (d) calculated stress and (e) piezo potential distribution for a similar area of the pure PVDF, 20% circular porous PVDF and 60% porous $FAPbBr_2$-I@PVDF film (porosity induced by 20 wt% of $FAPbBr_2I$).

The porosity and size of the pores can be well controlled *via* tuning the mass ratios (wt%) of the hybrid halide perovskites with the polymer. The corresponding surface morphologies revealed in the AFM images (Fig. S5f, ESI†) show that the pore diameter gradually increases to approximately ≈7 μm at 30 wt% of $FAPbBr_2I$. During the crystallization process, the increase in mass ratios should led to the agglomeration of $FAPbBr_2I$ NPs. The reason should be the aforementioned strong dipolar interactions between the FA^+ cations and the anionic fluorine ($-CF_2-$) groups of the PVDF.[48,49]

It has been investigated that the porosity in ferroelectric polymers will remarkably boost the piezoelectric potential by forming stress concentration centres around each pore. A PNG model for the perovskite/polymer composite was constructed to reveal the effects of self-assembled highly-porous characteristics on the output piezo-potential, and simulated using COMSOL Multiphysics 5.3. The simulation results compared with those of pure (solid without pores) PVDF films and 20% circular shaped porous PVDF films (circular shapes were adopted from the ZnO NPs). Fig. 2d clearly shows that, under uniaxial compressive stress of 800 kPa, the induced displacement of the three different PNG models (the same film thickness of 30 μm) is drastically different. The pure PVDF film is the least deformed, whereas the hybrid halide perovskite induced porous PVDF is the most deformed. It is evident that the pore position and size, influences the mechanical stress distribution, which is attributed to the increase in the average stress distribution profiles inside the films. From the finite element calculation (along the cut lines in Fig. S6b and c, ESI†), the stress inside the pure PVDF film is quite uniform under uniaxial vertical stress. In contrast, in the circular porous PVDF structure, the stress distribution is asymmetric in nature. Compared to the pure PVDF the stress distribution in the circular porous PVDF model is extremely disrupted by the presence of pores. In such circular porous structures (the middle model of Fig. 2d), the stress is mainly confined around each pores but is particularly higher along the direction of the applied force, namely, at the top and bottom pore sides. Therefore, the localized compressive strain of each pores results in a bulk film strain mainly in the vertical direction (*x*-direction strain $S_1 \approx 0\%$, *y*-direction strain $S_2 \approx 3.4\%$) and modifies the internal coupling.

Excitingly, unlike the uniform and circular porous PVDF (the deformation mainly occurred in the vertical direction), the highly ordered porous structure (the right most model of Fig. 2d) of the $FAPbBr_2I$@PVDF film is not only deformed along the vertical direction ($S_2 \approx 17\%$) but also significantly elongated along the horizontal direction ($S_1 \approx 57\%$). The stress concentration spots at the top exert a pushing force on the pores of the perovskite/polymer composite, inducing a relaxing strain on the two sides. Fig. S6b† (the right most model) shows the linear stress-enhancing characteristics of this larger pore to the sidewall of the structure. This phenomenon is similar to the flex-tensional mechanism,[52,53] which underlines the structural

modification of the mechanical body that could further amplify the applied vertical stress into the horizontal direction.

Since the strain-induced piezo potential is a collective outcome from the strains around each of the pores, the piezoelectric potential in the circular porous PVDF structure is therefore higher (Fig. 2e) than that in the non-porous PVDF piezoelectric films. The vibration-induced electric displacement D_3 (charge per unit area) is calculated by

$$D_3 = e_{333}S_{33} + |e_{331}|S_{31} \quad (2)$$

where e_{331} and e_{333} are the piezoelectric constants[54] and S_{31} and S_{33} are induced strains along the horizontal and vertical directions, respectively (Note 1, ESI†). It is clear that the D_3 of the $FAPbBr_2I$@PVDF composite film is synergistically influenced by the bidirectional (horizontal and vertical) strains S_1 ($\approx$57%) and S_2 ($\approx$17%). Therefore, the proposed novel P-PNG structure greatly increases the strain-induced piezo-potential or voltage output (according to the parallel plate capacitor model, $V = Q/C$, where Q is the total induced charge and C is the device capacitance), which was confirmed by the finite element simulation in Fig. 2e. It demonstrates the maximum piezoelectric potential of $\approx$40 V for $FAPbBr_2I$@PVDF composite films, which is $\approx$11 V and $\approx$15 V for pure and 20% porous PVDF films, respectively (with the same applied stress of 800 kPa). It should be noted that an array of such a highly ordered pores (Fig. S7, ESI†) in the P-PNG, would generate even higher potential than a structure having a single of such pores (the right most model in Fig.-S7b†). In the array with such a larger pore, the wall of the inner pore structures are highly compressed due to the bidirectional stress (indicated by the arrows in Fig. S7a, ESI†). Between the interpore distance, the boosted stress is further improving the piezoelectric potential of the film. Yuan *et al.* also enhanced the total piezo potential of a 6-layer PVDF-TrFE (trifluoro ethylene) based PNGs by 2.2 times, by making a rugby-ball-shaped PNG structure to utilize this flex-tensional strain effect.[19] Our approach is another promising way to develop new PNGs based on the amplified mechanical strain of a particular composite piezoelectric film and to realize a compact and flexible power source for next-generation micro/nanodevices.

2.2 Energy harvesting performance of the P-PNGs

The highly porous $FAPbBr_2I$@PVDF film provides an excellent platform for developing scalable PNGs, which only need two thin metal electrodes (copper) on both sides. Exploiting the unique micro structure features along with the formation of beneficial $FAPbBr_2I$ nanocrystals, we investigated the effect on practical PNG performance. The device was placed on a hammer of an electrodynamic shaker and sandwiched by a 138 g metal block (stainless steel) on top (schematic illustration of testing set-up in Fig. S8, ESI†). The generated output voltage and current were measured from the periodic mechanical vibration produced by the electrodynamic shaker at various frequencies (10–50 Hz) and accelerations (1–2.5 G). We found an output voltage of $\approx$85 V (peak to peak) and short-circuit current of $\approx$30 μA (peak to peak), respectively, from an active device area of 3.8 cm × 3.8 cm at 30 Hz and 2 G (results are presented in Fig. S9a and b, ESI†). In Fig. S10a–e,† the electricity generation mechanisms of this P-PNG device are schematically illustrated from the stress mapping by employing finite element simulation (COMSOL Multiphysics 5.3). When there is no applied electric field, the net dipole moment inside the film is almost zero (Fig. S10a, ESI†). By applying a high electric field (50–120 V μm^{-1}) for 2–3 hours, dipoles are aligned to the direction of the electric field (Fig. S10b, ESI†). Now, if a compressive force is applied to the device, the net polarization changes in the composite film due to the flex-tensional strain, thus producing piezoelectric potential (Fig. S10c, ESI†). We predict that due to rapid change in the net dipole moment by the flex-tensional mechanism will promote a polarization change in the poled P-PNG, yielding an even higher potential.[55,56] If the two electrodes are connected to each other, then an electric current will flow to balance this piezo potential. While releasing the force, the piezo potential returns to zero because of the diminished film strain, and then the accumulated electrons will flow back (Fig. S10d, ESI†). Due to the formation of larger porous structures, the piezoelectric film could undergo an additional damping cycle, leading to the observation of a second output current pulse (Fig. S10e, ESI†). As discussed earlier that the pore size (and thus porosity) in the $FAPbBr_2I$@PVDF composite film increases with the concentration of $FAPbBr_2I$ precursors, which plays an important role in the PNG device performance. We found an interesting trend, that the output voltage and current increases with the composition of $FAPbBr_2I$ (up to $\approx$85 V and $\approx$30 μA at 20 wt%) and decreases afterwards (Fig. S11a and b,† ESI). The possible reasons are: firstly, PVDF per unit volume is greatly reduced due to the very high porosity. Secondly, the film impedance is reduced by higher mass ratios (>20 wt%) of $FAPbBr_2I$, as a result, causing the earlier dielectric breakdown before maximum polarization charges are achieved by electrical poling. Thirdly, the defects generated by the agglomeration of $FAPbBr_2I$ NPs. Therefore, the device with 20 wt% of $FAPbBr_2I$ demonstrated highest output performance, and after the certain threshold margin, the device performance starts to degrade with further addition of excess $FAPbBr_2I$ NPs. The highest measured output voltage and current of the P-PNG with 20 wt% $FAPbBr_2I$ was compared with the pure and 20% circular porous PVDF based PNG devices (Fig. 3a and b). Notably, the output voltage and current of the 20 wt% P-PNGs are boosted by $\approx$ 5 times and $\approx$15 times, respectively, compared to those of the pure PVDF based PNG model ($\approx$17 V, and $\approx$2 μA).They are also substantially higher than those of the 20% circular porous PVDF PNG ($\approx$40 V, $\approx$6 μA). The generated electricity of the P-PNG originated from the inherent piezoelectric polarization[57–64] was verified from the output polarity switching (Fig. 3c & ESI movie†) clearly showing the expected output reversal. We sought further evidence by investigating the intrinsic material properties to explain the sharp enhancement in the output current of the P-PNG device. The relative permittivity of the porous PVDF and 20 wt% $FAPbBr_2I$@PVDF films were measured in a frequency range of 1 kHz to 1 MHz (Fig. 3d). For both of the films, at the lower frequency regime, permittivity is high at the beginning due to the interfacial polarization effect[65] between

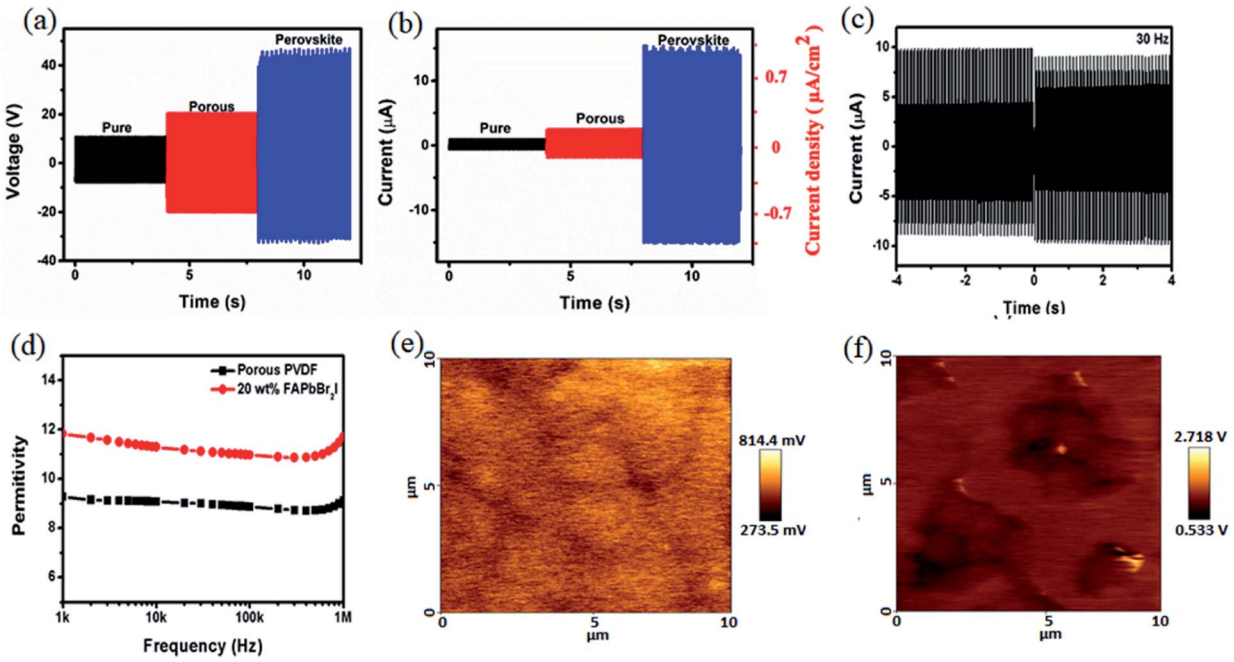

Fig. 3 The output performance of P-PNGs (a) V_{oc} and (b) I_{sc} of PNGs made from pure PVDF, porous PVDF (with ZnO nanoparticles) and $FAPbBr_2I$@PVDF composite films. For the porous PVDF, and $FAPbBr_2I$@PVDF composite films, the original mass ratios of nanoparticles inside the final films are 20 wt%. (c) Polarization verification of the P-PNGs by switching test; (d) relative permittivity of the porous and 20 wt% $FAPbBr_2I$@PVDF composite films; KPFM images of the (e) porous and (f) 20 wt% $FAPbBr_2I$@PVDF composite films.

the nanoparticles and polymer interface, which arises from the free carriers in the polymer material. However, with an increase in the applied electric field frequency, the interfacial polarization cannot cope up with the frequency change, which results in the decreased permittivity. Lastly the increasing pattern of the relative permittivity could be correlated with the arising of a high frequency stray capacitance during the measurements. The higher permittivity of the $FAPbBr_2I$@PVDF film ($\approx$12 at 1 kHz) enhances the piezoelectric performance, as it increases the piezoelectric coefficient (D_3).[66–68] In addition, the enhanced permittivity of $FAPbBr_2I$ perovskites give rise to the output current by reducing the internal impedance (Z) of the film

$$Z = R - J\frac{d}{2\pi A\varepsilon_0\varepsilon_r} \quad (3)$$

where, R is the film resistance, d the thickness, A the area, ε_0 the vacuum permittivity and ε_r the relative permittivity.

The charges due to the internal polarization are also affected by the relative permittivity of $FAPbBr_2I$. We measured the surface potential of the $FAPbBr_2I$@PVDF film by employing Kelvin probe force microscopy (KPFM). The relationship between the permittivity and polarization can be expressed as[69]

$$\vec{P} = \varepsilon_0(\varepsilon_r - 1)\vec{E} \quad (4)$$

where, $\vec{P}$ is the electric polarization within the material, ε_0 the permittivity of free space (8.854×10^{-12} F m^{-1}), ε_r the relative permittivity and $\vec{E}$ the electric-field. From eqn (4), the higher permittivity of the composite film due to the presence of perovskite will certainly change the strain induced electric field inside the composite film, and as a result the magnitude of the surface potential will be different. In general, for perovskite PNGs, the surface potential is of particular interest because it affects band bending and carrier transport at the interfaces.[70–74] By measuring the contact potential difference using a platinum (Pt) KPFM tip ($\approx$20 nm radius) in intermittent contact mode, the average surface potential of $FAPbBr_2I$@PVDF was found to be 1.1 V, which is more than twice that of porous PVDF (Fig. 3e and f). The observed variation in the average surface potential in $FAPbBr_2I$@PVDF film was very small (<100 mV), which eliminates possible surface contamination by the remnant precursors-formamidinium iodide (FAI), or lead bromide ($PbBr_2$).

The combination of high permittivity and the porosity mediated spongy type mechanical property made the $FAPbBr_2I$@PVDF thin film a promising candidate for harvesting mechanical energy from a wide range of environmental vibrations. The ambient vibration dependent output voltage and current of the P-PNGs (Fig. S12, ESI†) were measured. By keeping the force constant, we varied the frequency of the electrodynamic shaker from 10–50 Hz by a controller unit (Vibration Research's VR 9500 Revolution). Maximum output was obtained at 30 Hz, corresponding to the resonant condition in which the electromechanical coupling is the greatest. To evaluate the flexibility of the device, we applied a periodic bending force at a constant strain rate (15.5 cm s^{-1}) and measured the output voltage and current. The peak to peak output voltage was 14 V, and the current was 0.3 μA (ESI movie & Fig. S13a, b, ESI†), which can be enhanced further by increasing the bending radius.[40]

2.3 Applications of P-PNGs as a sustainable power source in the IoT

Despite vast efforts in the past decade, the implementation of composite PNGs, especially in real-time applications, is still limited. To address these limitations, we employed our novel flexible P-PNGs as a power source to implement a true SIWEN for the distributed IoT network. This SIWEN can remotely communicate with any Bluetooth-compatible personal electronics to transfer data from many distributed sensors. The functional block diagram of the SIWEN is shown in Fig. 4. The SIWEN incorporates a rectification unit, two-stage energy transfer system, regulated switches, and a low-power system on chip (SoC) for conditioning the sensor signal and transmitting it to a remote end receiver (more details of SIWEN are elucidated in Note 2 & Fig. S14, ESI†). In Fig. 4, a P-PNG is exemplified both as an electrical power source and sensor, which is capable of harnessing mechanical energy from wide range of vibration sources (*e.g.* human motion, vibration of aircrafts and automobiles). However, during the experiment, an electrodynamic shaker was used to generate mimic vibrations at 30 Hz and 2 G (ESI Movie†).

Before integrating the P-PNG with SIWEN, a practical load-driving capability was confirmed. The maximum instantaneous power delivered to the load was measured from the output currents of the P-PNG with a wide range of external load resistances (100 kΩ to 80 MΩ). A peak output power of ≈105 μW and a power density of 10 μW cm^{-2} were obtained at a load resistance of 7 MΩ (Fig. 5a). The energy harnessed by the P-PNG is being stored to powering up the SIWEN to initiate data transfer.

The measured charging characteristics of the two-stage energy transfer system enabled by two capacitors (C_p) are shown in Fig. 5b. When the voltage of an input capacitor (1 μF) reaches ≈5 V, which is regulated by a Zener diode, it discharges energy through a buck converter module to an output capacitor (220 μF). The buck converter module consists of two metal oxide semiconductor field-effect transistor (MOSFET) switches. After the output voltage of the 1 μF input capacitor dropped down to a regulated voltage of ≈2–3 V, the 220 μF output capacitor is disconnected from it by the MOSFET switches and the input capacitor stops discharging and starts to be charged. In this manner the output capacitor is charged until ≈3.1 V with high energy transfer efficiency, and can power up any electronics node. Another P-PNG (P-PNG sensor) incorporated in the SIWEN as a sensing unit (ESI Movie†), is connected with an analogue to digital converter (ADC) of the SoC *via* an impedance matching bridge. Immediately after reaching the output voltage of the 220 μF capacitor to 3.1 V, a trigger signal turns on a switch through which the output capacitor discharges energy to power-up the SoC and transmits the digital sensor data from the P-PNG sensor to a remote receiver. The full operation of energy harvesting, energy storing, data collecting and wireless transmitting were demonstrated and recorded (ESI Movie†). Fig. 5c shows, two smartphones receiving the transmitted data from the SIWEN and decode the mimic sensor signals (obtained from the P-PNG sensor).

To assess more versatile applicability, the P-PNGs were used in harnessing vibration from an automobile vehicle (the car in is park mode while the engine is turned on as shown in the ESI Movie†). Fig. 5d depicts the measured output voltage from the P-PNG, mounted on the car (while the engine is running), where device output reflects the acceleration and rotational speed-dependent vibration pattern of the engine. After the engine is turned on, the rpm (revolutions per minute) was varied from a range of 1–1.5, 1.5–2, 2–2.5 kilo revolutions per minute (krpm) while maintaining a constant acceleration between each rpm regimes. Initially, a peak-to-peak voltage of ≈13 V was measured, which is attributed to the abrupt engine vibration when getting started. Later, the P-PNG output dropped, due to a gradual decrease in the vibration magnitude in the higher rpm regimes.

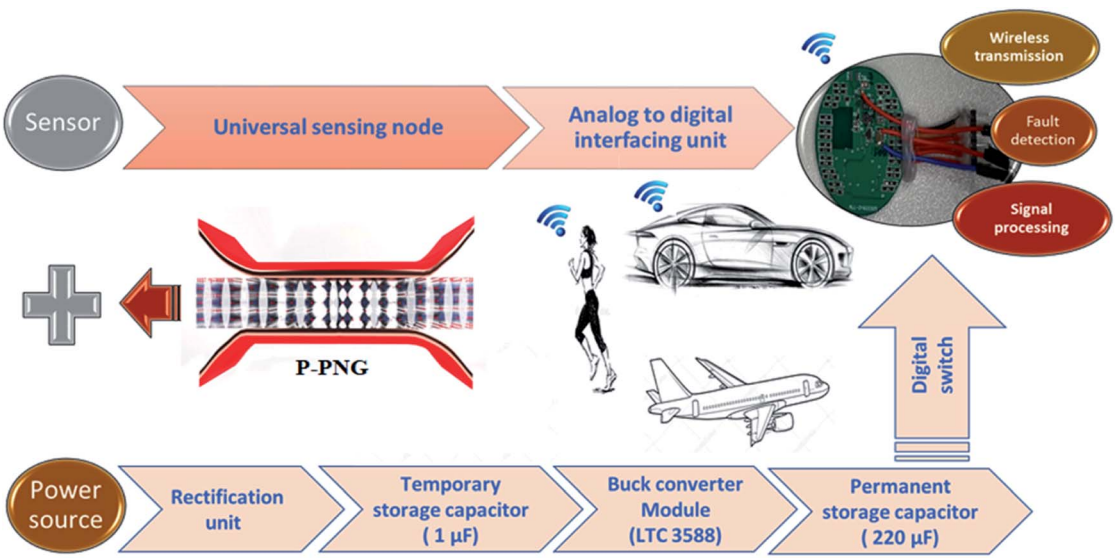

Fig. 4 Framework of the self-powered integrated wireless electronics node (SIWEN) by simultaneously using the P-PNGs as a power-source and a sensor.

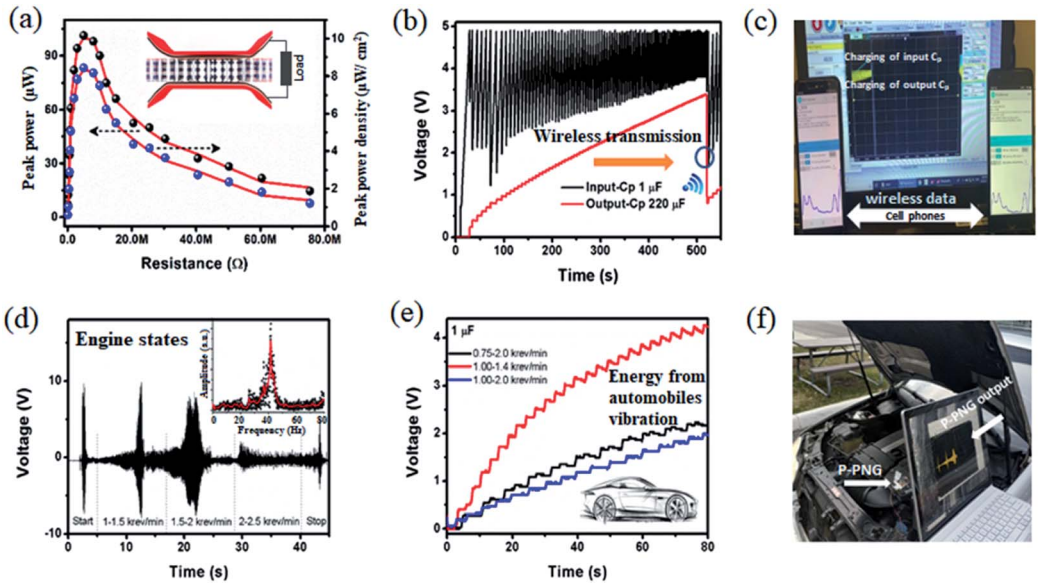

Fig. 5 Application of the P-PNGs for IoT (a) the measured output power of the P-PNG with an applied acceleration of 2 G (30 Hz). The used load was a metal block of 138 g; (b) charging characteristics of the input (1 μF) and output capacitor (220 μF) of the SIWEN; (c) the digital photo shows the sensor signal received by the cell-phone; (d) SIWEN used for car engine states detection at a parking condition (inset shows the corresponding frequency domain distribution *via* fast Fourier transform); (e) charging of a commercial capacitor (1 μF) by a single P-PNG while exciting by an automobile engine (Mercedes-Benz car); (f) the corresponding digital photo of engine vibration detection.

We also performed a fast Fourier transform (inset of Fig. 5d) revealing the major contribution of the device output produced from the vibration components of approximately 40 Hz, which is close to the resonance frequency of the P-PNG. By harnessing energy from such minute engine vibrations, a commercial capacitor of 1 μF was charged up to 4 V in ≈1 minute (Fig. 5e & ESI Movie†). The capacitor was continuously charged up by switching the car rpm back and forth between 1–1.4 krpm (red curve), 1–2 krpm (blue curve) and 0.75–2 krpm (black curve).

The best charging performance at 1–1.4 krpm is attributed to the highest acceleration and more frequent excitation (due to lower rpm switching time) to the capacitor. For the other two wider rpm regimes, acceleration is lower and their longer rpm switching time allows the capacitor to further discharge its energy. Hence, scalable P-PNGs are critical for industrially viable nanogenerator applications. To evaluate the scalability of the high-performance P-PNGs, we fabricated a large-area device (15 cm × 15 cm). Therefore, in reference to the ESI movie† it is visible that a small force applied by the touch of a human hand is capable of generating sufficient electricity to drive a LED, which also indicates the efficiency of the P-PNGs as a large area energy harnessing device.

3. Conclusion

To summarize we discovered a novel self-assembled highly porous phenomenon in a composite piezoelectric polymer film (PVDF in this case), by employing new hybrid halide perovskites ($FAPbBr_2I$) precursors, which is significant for designing high-performance nanogenerators for next-generation self-powered devices. We successfully fabricated an efficient, flexible and all-solution processed perovskite-piezoelectric nanogenerator (P-PNGs). Because of the enlarged film strain of the self-assembled highly ordered porous scaffold (PVDF) and the enhanced relative permittivity of the novel perovskite $FAPbBr_2I$, the composite material's piezoelectricity was dramatically boosted, yielding a strain-induced piezo potential of 85 V (≈5 times greater than PVDF PNGs) and a current of ≈30 μA (≈15 times more than PVDF PNGs), with an applied load of 138 g. A very high peak output power density of 10 μW cm^{-2} (across a resistance of 7 MΩ) was recorded to implement our novel P-PNGs in a broad range of practical applications. The experimental results were supported by the numerical simulation of three different PNG device models (pure PVDF, circular porous PVDF and the perovskite–polymer composite film). A self-powered universal wireless electronics node (SIWEN) capable of communicating remotely with personal electronics was demonstrated by using the P-PNG as an alternative means of a battery. The P-PNG could also generate electricity by harnessing energy from automobile vibrations and biomechanical motion which can be easily extended to many applications as well. This research reveals the underlying mechanisms for the performance enhancement observed in the P-PNGs based on the novel perovskite/polymer composite film. This in return shows that the results pave a way to achieve the practical implementation of self-powered technologies.

4. Experimental section

4.1 Synthesis of the pure PVDF films

To prepare the PVDF solution, PVDF was purchased as a powder form (Sigma Aldrich) and was dissolved in *N*,*N*-DMF (*N*,*N*-

dimethylformamide ≥99%, Sigma Aldrich) solvent (10 wt%) by stirring for 12 hours at 40 °C. The temperature was maintained at 40 °C and was used to prevent agglomeration and achieving better dissolution. To prepare the PVDF film, the solution was drop casted on a standard glass wafer that was placed on a very flat hotplate. The sides of the glass substrates were covered with polyamide tape, to prevent the solution from flowing outwards. Before starting the annealing process, the solution was kept under ambient conditions for 30 minutes for degassing. To form the spontaneous electroactive β-phase in the PVDF, the curing temperature was adjusted carefully and kept at 80 °C for 1 hour. Then as grown thin film (≈40–50 μm) was peeled off from the glass substrate. The formation of the β-phase in the PVDF was confirmed by FTIR spectrum analysis (Fig. S1c, ESI†) and the surface morphology was investigated by using a scanning electron microscope (SEM) (Fig. S1a and b,† ESI). Finally, a high voltage electrical poling (50–120 V μm^{-1}) was performed for 2–4 hours to align the electric dipoles. For the high-voltage poling purpose-two gold coated copper electrodes were prepared *via* the electroplating method. To minimize the negative influence of the ambient moistures or the dust particles, the electrical poling was performed in a vacuum box. After that, to make the PNG, the films were placed between two copper tapes, and thermally laminated between two polyester substrates.

4.2 Synthesis of the porous PVDF films

PVDF powder was dissolved in *N*,*N*-dimethylformamide (DMF) by stirring the solution for 12 hours at 40 °C. To create different porosities, zinc oxide (ZnO) nanoparticles (NPs) (35–45 nm, US Research Nanomaterials, Inc.) were dispersed into the PVDF solution and again stirred at 40 °C for 24 hours. The mass ratios between the PVDF and ZnO NPs (20 wt% for this experiment) were adjusted to create different pores inside the PVDF to achieve a uniformly mixed PVDF–ZnO composite solution, it was further treated in an ultrasonic bath for 1 hour. Then the uniform solution was drop casted onto a glass substrate and degassed for 30 minutes. The solution was cured at 75 °C inside a vacuum oven for 30 minutes. Afterward, the PVDF–ZnO composite film was peeled off from the glass substrate (Fig. S2a and b,† ESI for the surface and cross-sectional morphology). To obtain the porosity inside the PVDF, one-step etching of the ZnO NPs was performed in an ultrasonic bath by immersing the PVDF–ZnO composite film in a 37 wt% HCl solution for 4 hours. Then the porous film was cleaned with DI water, and dried in a nitrogen filled oven at 60 °C for 3 hours (Fig. S2c–e† for the surface morphology). Finally, high-voltage electrical poling (50–120 V μm^{-1}) was performed for 2–4 hours to align the dipole. Then the films were placed between two copper tapes and thermally laminated to encapsulate them between the polyester substrates.

4.3 Synthesis of the $FAPbBr_2I$@PVDF composite films

The $FAPbBr_2I$ precursor solution was prepared by dissolving FAI (formamidinium iodide ≥99%, Sigma-Aldrich) and $PbBr_2$ (lead(II) bromide ≥98%, Sigma-Aldrich) at an equal molar ratio (0.5 : 0.5) in an *N*,*N*-DMF (*N*,*N*-dimethylformamide ≥99%, Sigma-Aldrich) solvent, followed by stirring at 60 °C for 12 hours. The PVDF solution was dissolved in *N*,*N*-DMF with constant stirring at 50 °C for 24 hours. The final concentrations of $FAPbBr_2I$ and PVDF in DMF were kept at 20 wt% and 10 wt%, respectively. Then, the $FAPbBr_2I$@PVDF composite precursor solutions were prepared by homogeneously mixing 20 wt% $FAPbBr_2I$ and 10 wt% PVDF. To optimize the concentration, the 10 wt%, 20 wt%, and 30 wt% composite solutions were synthesized. Then the mixed solution was drop-casted onto a glass substrate and stored for approximately 1 hour for the degassing process. Immediately followed by annealing at 120 °C, the highly crystalline composite films were obtained after 2–3 hours. To align the dipoles in the $FAPbBr_2I$@PVDF film, high-voltage electrical poling was completed with an electric field of 50–120 V μm^{-1} for 2–3 hours. After the poling, the films were sandwiched between two copper electrodes. Finally, the sandwiched structure of the polyester/copper/$FAPbBr_2I$–PVDF/copper/polyester film was pressed through thermal lamination, which eliminates air gaps and provides uniform adhesion between the copper electrodes and the piezoelectric film.

4.4 Characterization and measurements

To investigate the crystallinity of the hybrid halide into the ferroelectric PVDF scaffold we performed X-ray diffraction (XRD) analysis. A Bruker D8 DISCOVER was used with a Cu Kα radiation source ($\lambda = 1.54$ Å) to scan the optimized thin film samples (25 wt% $FAPbBr_2I$–PVDF) from an angular range of zero to seventy degrees. Fourier transform infrared spectroscopy (Nicolet iS50) was employed to confirm the ferroelectric β-phase formation inside the porous PVDF and hybrid halide-embedded PVDF film by measuring the characteristic absorbance peak in a wavenumber range from 400 to 1000 cm^{-1}. The dielectric properties of the samples (*C*–*V* characteristics) were measured using a Keithley-4200 semiconductor parameter analyzer. JSM-7200F field-emission scanning electron microscopy tools were used to obtain surface morphologies and nanoparticles distributions inside PVDF were mapped by analysing energy dispersive X-rays in a cleanroom environment (Class-100). The AFM and KPFM images were captured using a JPK Nanowizard II, configured in intermittent-contact mode (a scan rate of 0.3 Hz). For the KPFM imaging, a cantilever probe (spring constant 42 N m^{-1}) with a platinum-coated tip (radius < 20 nm) was used to probe a grounded sample. We maintained constant tip–sample interaction with a phase-locked loop and the internal reference of the lock-in amplifier was an applied AC voltage (3 kHz) to the sample surface. To study the electrical output performance of the P-PNGs an electrodynamic shaker (Lab Works Inc.) was used, controlled by a power amplifier and a controller. A digital oscilloscope (Tektronix 2004 C) and a low-noise current preamplifier (SR 570, Stanford Research Systems Inc.) were used to measure the electrical signal output from the nanogenerators.

Conflicts of interest

There are no conflicts to declare.

Acknowledgements

This research was supported by the Natural Sciences and Engineering Research Council of Canada (NSERC); Ontario Centres for Excellence (OCE), Canada; and Shimco North America Inc., Cambridge, Ontario, Canada.

Notes and references

1 C. Soci, A. Zhang, B. Xiang, S. A. Dayeh, D. Aplin, J. Park, X. Bao, Y.-H. Lo and D. Wang, *Nano Lett.*, 2007, **7**, 1003.
2 Y. Qi and M. C. Mcalpine, *Energy Environ. Sci.*, 2010, **3**, 1275.
3 R. S. Yang, Y. Qin, L. M. Dai and Z. L. Wang, *Nat. Nanotechnol.*, 2009, **4**, 34.
4 M. Y. Choi, D. Choi, M. J. Jin, I. Kim, S. H. Kim, J. Y. Choi, S. Y. Lee, J. M. Kim and S. W. Kim, *Adv. Mater.*, 2009, **21**, 2185.
5 T. Xu, X. Ding, Y. Huang, C. Shao, L. Song, X. Gao, Z. Zhang and L. Qu, *Energy Environ. Sci.*, 2019, **12**, 972.
6 Y. F. Hu, Y. Zhang, C. Xu, L. Lin, R. L. Snyder and Z. L. Wang, *Nano Lett.*, 2011, **11**, 2572.
7 C. L. Sun, J. Shi, D. J. Bayerl and X. D. Wang, *Energy Environ. Sci.*, 2011, **4**, 4508.
8 G.-T. Hwang, H. Park, J.-H. Lee, S. Oh, K.-I. Park, M. Byun, H. Park, G. Ahn, C. K. Jeong, K. No, H. Kwon, S.-G. Lee, B. Joung and K. Jae, *Adv. Mater.*, 2014, **26**, 4880.
9 S. N. Cha, S. M. Kim, H. Kim, J. Ku, J. I. Sohn, Y. J. Park, B. G. Song, M. H. Jung, E. K. Lee, B. L. Choi, J. J. Park, Z. L. Wang, J. M. Kim and K. Kim, *Nano Lett.*, 2011, **11**, 5142.
10 S. Lu, Q. Liao, J. Qi, S. Liu, Y. Liu, G. Zhang and Y. Zhang, *Nano Res.*, 2016, **9**, 372.
11 J. Li, S. Chen, W. Liu, R. Fu, S. Tu, Y. Zhao, L. Dong, B. Yan and Y. Gu, *J. Phys. Chem. C*, 2019, **123**, 11378.
12 Z. L. Wang and J. Song, *Science*, 2006, **312**, 242.
13 Y. Su, K. Gupta, Y. Hsiao, R. Wang and C. Liu, *Energy Environ. Sci.*, 2019, **12**, 410.
14 Y. Mao, P. Zhao, G. McConohy, H. Yang, Y. Tong and X. Wang, *Adv. Energy Mater.*, 2014, **4**, 1301624.
15 G. Zhang, P. Zhao, X. Zhang, K. Han, T. Zhao, Y. Zhang, C. K. Jeong, S. Jiang, S. Zhang and Q. Wang, *Energy Environ. Sci.*, 2018, **11**, 2046.
16 C. R. Bowen, H. A. Kim, P. M. Weaver and S. Dunn, *Energy Environ. Sci.*, 2014, **7**, 25.
17 D. Chen, K. Chen, K. Brown, A. Hang and J. X. J. Zhang, *Appl. Phys. Lett.*, 2017, **110**, 153902.
18 Z. Zhang, C. Yao, Y. Yu, Z. Hong, M. Zhi and X. Wang, *Adv. Funct. Mater.*, 2016, **26**, 6760.
19 X. Yuan, X. Gao, J. Yang, X. Shen, Z. Li, S. You, Z. Wang and S. Dong, *Energy Environ. Sci.*, 2020, **13**, 152.
20 J.-H. Lee, K. Y. Lee, M. K. Gupta, T. Y. Kim, D.-Y. Lee, J. Oh, C. Ryu, W. J. Yoo, C.-Y. Kang, S.-Y. Yoon, J.-B. Yoo and S.-W. Kim, *Adv. Mater.*, 2013, **26**, 765.
21 J. Zhu, W. Song, F. Ma and H. Wang, *Mater. Res. Bull.*, 2018, **102**, 130.
22 K. Zhang, S. Wang and Y. Yang, *Adv. Energy Mater.*, 2017, **7**, 1601852.
23 C.-H. Wang, W.-S. Liao, Z.-H. Lin, N.-J. Ku, Y.-C. Li, Y.-C. Chen, Z. L. Wang and C.-P. Liu, *Adv. Energy Mater.*, 2014, **4**, 1400392.
24 X. Xue, Y. Nie, B. He, L. Xing, Y. Zhang and Z. L. Wang, *Nanotechnology*, 2013, **24**, 22.
25 Y. Fu, W. Zang, P. Wang, L. Xing, X. Xue and Y. Zhang, *Nano Energy*, 2014, **8**, 34.
26 S. A. Han, T.-H. Kim, S. K. Kim, K. H. Lee, H.-J. Park, J.-H. Lee and S.-W. Kim, *Adv. Mater.*, 2018, **30**, 1800342.
27 A. Mahmud, A. A. Khan, P. Voss, T. Das, E. Abdel-Rahman and D. Ban, *Adv. Mater. Interfaces*, 2018, **5**, 1801167.
28 J. H. Jung, M. Lee, J. Hong, Y. Ding, C. Chen, L. Chou and Z. L. Wang, *ACS Nano*, 2011, **5**, 10041.
29 S. Xu, Y.-W. Yeh, G. Poirier, M. C. Mcalpine, R. A. Register and N. Yao, *Nano Lett.*, 2013, **13**, 2393.
30 G. Romano, G. Mantini, A. D. Carlo, A. D'Amico, C. Falconi and Z. L. Wang, *Nanotechnology*, 2011, **22**, 465401.
31 K. I. Park, S. Xu, Y. Liu, G. T. Hwang, S. J. L. Kang, Z. L. Wang and K. J. Lee, *Nano Lett.*, 2010, **10**, 493.
32 C. K. Jeong, I. Kim, K. I. Park, M. H. Oh, H. Paik, G. T. Hwang, K. No, Y. S. Nam and K. J. Lee, *ACS Nano*, 2013, **7**, 11016.
33 S.-H. Shin, Y.-H. Kim, M. H. Lee, J.-Y. Jung, J. H. Seol and J. Nah, *ACS Nano*, 2014, **8**, 10844.
34 C. Baek, J. H. Yun, J. E. Wang, C. K. Jeong, K. J. Lee, K. I. Park and D. K. Kim, *Nanoscale*, 2016, **8**, 17632.
35 K. I. Park, M. Lee, Y. Liu, S. Moon, G. T. Hwang, G. Zhu, J. E. Kim, S. O. Kim, D. K. Kim, Z. L. Wang and K. J. Lee, *Adv. Mater.*, 2012, **24**, 2999.
36 C. K. Jeong, K. I. Park, J. Ryu, G. T. Hwang and K. J. Lee, *Adv. Funct. Mater.*, 2014, **24**, 2620.
37 K. Shi, B. Sun, X. Huang and P. Jiang, *Nano Energy*, 2018, **52**, 153.
38 S. K. Ghosh, A. Biswas, S. Sen, C. Das, K. Henkel, D. Schmeisser and D. Mandal, *Nano Energy*, 2016, **30**, 30621.
39 Y. L. Zhao, Q. L. Liao, G. J. Zhang, Z. Zhang, Q. J. Liang, X. Q. Liao and Y. Zhang, *Nano Energy*, 2015, **11**, 719.
40 B. S. Lee, J. Yoon, C. Jung, D. Y. Kim, S. Y. Jeon, K. H. Kim, J. H. Park, H. Park, K. H. Lee, Y. S. Kang, J. H. Park, H. Jung, W. R. Yu and S. G. Doo, *ACS Nano*, 2016, **10**, 2617.
41 E. J. Lee, T. Y. Kim, S. Kim, S. Jeong, Y. Choi and S. Y. Lee, *Energy Environ. Sci.*, 2018, **11**, 1425.
42 A. Sultana, M. Alam, P. Sadhukhan, U. K. Ghorai, S. Das, T. R. Middya and D. Mandal, *Nano Energy*, 2018, **49**, 380.
43 R. Ding, X. Zhang, G. Chen, H. Wang, R. Kishor, J. Xiao, F. Gao, K. Zeng, X. Chen, X. W. Sun and Y. Zheng, *Nano Energy*, 2017, **37**, 126.
44 V. Jella, S. Ippili, J.-H. Eom, J. Choi and S.-G. Yoon, *Nano Energy*, 2018, **53**, 46.
45 R. Ding, H. Liu, X. Zhang, J. Xiao, R. Kishor, H. Sun, B. Zhu, G. Chen, F. Gao, X. Feng, J. Chen, X. Chen, X. Sun and Y. Zheng, *Adv. Funct. Mater.*, 2016, **26**, 7708.
46 S. K. Ghosh, T. K. Sinha, B. Mahanty and D. Mandal, *Energy Technol.*, 2015, **3**, 1190.
47 A. Sultana, P. Sadhukhan, M. M. Alam, S. Das, T. R. Middya and D. Mandal, *ACS Appl. Mater. Interfaces*, 2018, **10**, 4121.

48 S. K. Ghosh, T. K. Sinha, B. Mahanty, S. Jana and D. Mandal, *J. Appl. Phys.*, 2016, **120**, 174501.
49 W. Ma, J. Zhang, S. Chen and X. Wang, *J. Macromol. Sci., Part B: Phys.*, 2008, **47**, 434.
50 H. L. W. Chan, M. C. Cheung and C. L. Choy, *Ferroelectrics*, 1999, **224**, 113.
51 Q. Zhou, Z. Bai, W. Lu, Y. Wang, B. Zou and H. Zhong, *Adv. Mater.*, 2016, **28**, 9163.
52 X. Li, M. Guo and S. Dong, *IEEE Trans. Ultrason. Ferroelectrics Freq. Contr.*, 2011, **58**, 698.
53 H.-X. Zou, W.-M. Zhang, W.-B. Li, Q.-H. Gao, K.-X. Wei, Z.-K. Peng and G. Meng, *Smart Mater. Struct.*, 2017, **26**, 11.
54 X. Gao, J. Wu, Y. Yu, Z. Chu, H. Shi and S. Dong, *Adv. Funct. Mater.*, 2018, **28**, 1706895.
55 W. Yang, W. Gong, C. Hou, *et al.*, *Nat. Commun.*, 2019, **10**, 5541.
56 Q. Sun, W. Seung, B. J. Kim, S. Seo, S.-W. Kim and J. H. Cho, *Adv. Mater.*, 2015, **27**, 3411.
57 Z. L. Wang, J. Chen and L. Lin, *Energy Environ. Sci.*, 2015, **8**, 2250.
58 W. L. Wang, K. J. Liao, C. G. Hu, S. X. Wang, C. Y. Kong and H. Y. Liao, *Sens. Actuators, A*, 2003, **108**, 55.
59 T. Quan and Y. Yang, *Nano Res.*, 2016, **9**, 2226.
60 W. Seung, H.-J. Yoon, T. Y. Kim, H. Ryu, J. Kim, J.-H. Lee, S. Kim, Y. K. Park, Y. J. Park and S.-W. Kim, *Adv. Energy Mater.*, 2017, **7**, 160098.
61 S. Qin, Q. Zhang, X. Yang, M. Liu, Q. Sun and Z. L. Wang, *Adv. Energy Mater.*, 2018, **8**, 1800069.
62 J. Luo, Z. Wang, L. Xu, A. Wang, K. Han, T. Jiang, Q. Lai, Y. Bai, W. Tang, F. R. Fan and Z. L. Wang, *Nat. Commun.*, 2019, **10**, 5147.
63 S. Priya, *J. Electroceram.*, 2007, **19**, 167.
64 A. A. Khan, A. Mahmud, S. Zhang, S. Islam, P. Voss and D. Ban, *Nano Energy*, 2019, **62**, 691.
65 S. Luo, Y. Shen, S. Yu, Y. Wan, W. Liao, R. Sun and C. Wong, *Energy Environ. Sci.*, 2017, **10**, 137.
66 A. Jain, K. J. Prashanth, A. K. Sharma, A. Jain and P. N. Rashmi, *Polym. Eng. Sci.*, 2015, **55**, 158.
67 R. Fries and A. J. Moulson, *J. Mater. Sci.: Mater. Electron.*, 1994, **5**, 238.
68 T. Zheng, H. Wu, Y. Yuan, X. Lv, Q. Li, T. Men, C. Zhao, D. Xiao, J. Wu, K. Wang, J. Li, Y. Gu, J. Zhu and S. J. Pennycook, *Energy Environ. Sci.*, 2017, **10**, 52.
69 S. Sadewasser, T. Glatzel, S. Schuler, S. Nishiwaki, R. Kaigawa and M. C. Lux-Steiner, *Thin Solid Films*, 2003, **257**, 431.
70 H. Röhm, T. Leonhard, M. J. Hoffmann and A. Colsmann, *Energy Environ. Sci.*, 2017, **10**, 950.
71 A. D. Schulz, H. Röhm, T. Leonhard, S. Wagner, M. J. Hoffmann and A. Colsmann, *Nat. Mater.*, 2019, **18**, 1050.
72 A. H. Rahmati, S. Yang, S. Bauer and P. Sharma, *Soft Matter*, 2019, **15**, 127.
73 A. Kuchler, *High Voltage Engineering: Fundamentals-Technology-Applications*, Springer Vieweg, Berlin, Germany 2018, p. 79.
74 K. Wang, Y. Hou, B. Poudel, D. Yang, Y. Jiang, M.-G. Kang, K. Wang, C. Wu and S. Priya, *Adv. Energy Mater.*, 2019, **9**, 1901753.